

Geophysical Research Letters®








RESEARCH LETTER

10.1029/2024GL109658

Special Collection:

Science from the Surface Water and Ocean Topography Satellite Mission

Phase-Resolved Swells Across Ocean Basins in SWOT Altimetry Data: Revealing Centimeter-Scale Wave Heights Including Coastal Reflection

Fabrice Ardhuin¹ , Beatriz Molero², Alejandro Bohé³, Frédéric Nougier¹ , Fabrice Collard⁴, Isabel Houghton⁵ , Andrea Hay^{6,7} , and Benoit Legresy^{6,7,8} 

Key Points:

- Surface Water Ocean Topography (SWOT) data provide the first open ocean spatial measurements of phase-resolved swells with wavelength 500–1,050 m
- Swells with heights as low as 3 cm are well detected by SWOT, allowing tracking across oceans
- Swell reflection off the coast can be separated from incident waves

Supporting Information:

Supporting Information may be found in the online version of this article.

Correspondence to:

F. Ardhuin,
ardhuin@ifremer.fr

Citation:

Ardhuin, F., Molero, B., Bohé, A., Nougier, F., Collard, F., Houghton, I., et al. (2024). Phase-resolved swells across ocean basins in SWOT altimetry data: Revealing centimeter-scale wave heights including coastal reflection. *Geophysical Research Letters*, 51, e2024GL109658. <https://doi.org/10.1029/2024GL109658>

Received 18 APR 2024

Accepted 7 AUG 2024

¹Laboratoire d'Océanographie Physique et Spatiale (LOPS), Univ. Brest, CNRS, IRD, Ifremer, IUEM, Brest, France, ²CLS, Ramonville St Agne, France, ³CNES, Toulouse, France, ⁴ODL, Locmaria-Plouzane, France, ⁵Sofar Ocean Technologies, San Francisco, CA, USA, ⁶School of Geography, Planning, and Spatial Sciences, University of Tasmania, Hobart, TAS, Australia, ⁷Commonwealth Scientific and Industrial Research Organisation, Hobart, TAS, Australia, ⁸Integrated Marine Observing System, Hobart, TAS, Australia

Abstract Severe storms produce ocean waves with periods of 18–26 s, corresponding to wavelengths 500–1,055 m. These waves radiate globally as swell, generating microseisms and affecting coastal areas. Despite their significance, long waves often elude detection by existing remote sensing systems when their height is below 0.2 m. The new Surface Water Ocean Topography (SWOT) satellite offers a breakthrough by resolving these waves in global sea level measurements. Here we show that SWOT can detect 25-s waves with heights as low as 3 cm, and resolves period and direction better than in situ buoys. SWOT provides detailed maps of wave height, wavelength, and direction across ocean basins. These measurements unveil intricate spatial patterns, shedding light on wave generation in storms, currents that influence propagation, and refraction, diffraction and reflection in shallow regions. Notably, the magnitude of reflections exceeds previous expectations, illustrating SWOT's transformative impact.

Plain Language Summary Wind storms at sea make waves that increase in size with wind speed, and with the distance over which the high winds have been able to amplify the waves. Once generated these waves propagate as swell around the world ocean: in that stage the wave period remains constant while the wave height decay away from the source. Waves with periods longer than 18 s are relatively infrequent, but they are an important source of seismic waves and coastal impacts. However, current remote sensing techniques miss long waves under 0.2 m high. The Surface Water Ocean Topography (SWOT) satellite mission changes this, spotting 25-s waves with heights as low as 3 cm. SWOT maps wave height, wavelength, and direction worldwide, revealing the influence of winds, currents and water depth. For example, We found stronger than expected coastal reflection, which will help revise wave forecasting models and their application in seismology.

1. Introduction

Only the most severe wind storms are capable of generating significant ocean wave energy with periods longer than 18 s, corresponding to a deep water wavelength of 500 m. Once generated, these waves radiate away from the storm as swell, following great circles across ocean basins (Munk et al., 1963), with a possible weak effect of currents on their propagation paths (Gallet & Young, 2014). The infrequent occurrences of these long period waves are found in ocean time series of surface elevation or near-surface pressure (Darbyshire, 1950), or land-based records of microseisms that provide a global but very indirect view of these long swells (Hanafin et al., 2012; Husson et al., 2012). Satellite observations are more direct but existing techniques, real aperture radar (Hauser et al., 2021; Jackson et al., 1985) and synthetic aperture radar (SAR) (Ardhuin et al., 2015; Hasselmann et al., 1985), are less reliable at detecting long waves with heights under 0.2 m.

The recently launched Surface Water Ocean Topography (SWOT) satellite mission uses a completely new type of instrument, a Ka-band Radar Interferometer (KaRIN) that consists of a pair of SARs that provides across-track interferometry from a single satellite pass, as described by Fu et al. (2024). SWOT has a unique capability of resolving kilometer-scale oscillations in global measurements of sea surface height (SSH) that can be used to map long swell parameters in unprecedented detail. Over the open ocean, SWOT provides measurements of radar

© 2024. The Author(s).

This is an open access article under the terms of the [Creative Commons Attribution License](https://creativecommons.org/licenses/by/4.0/), which permits use, distribution and reproduction in any medium, provided the original work is properly cited.

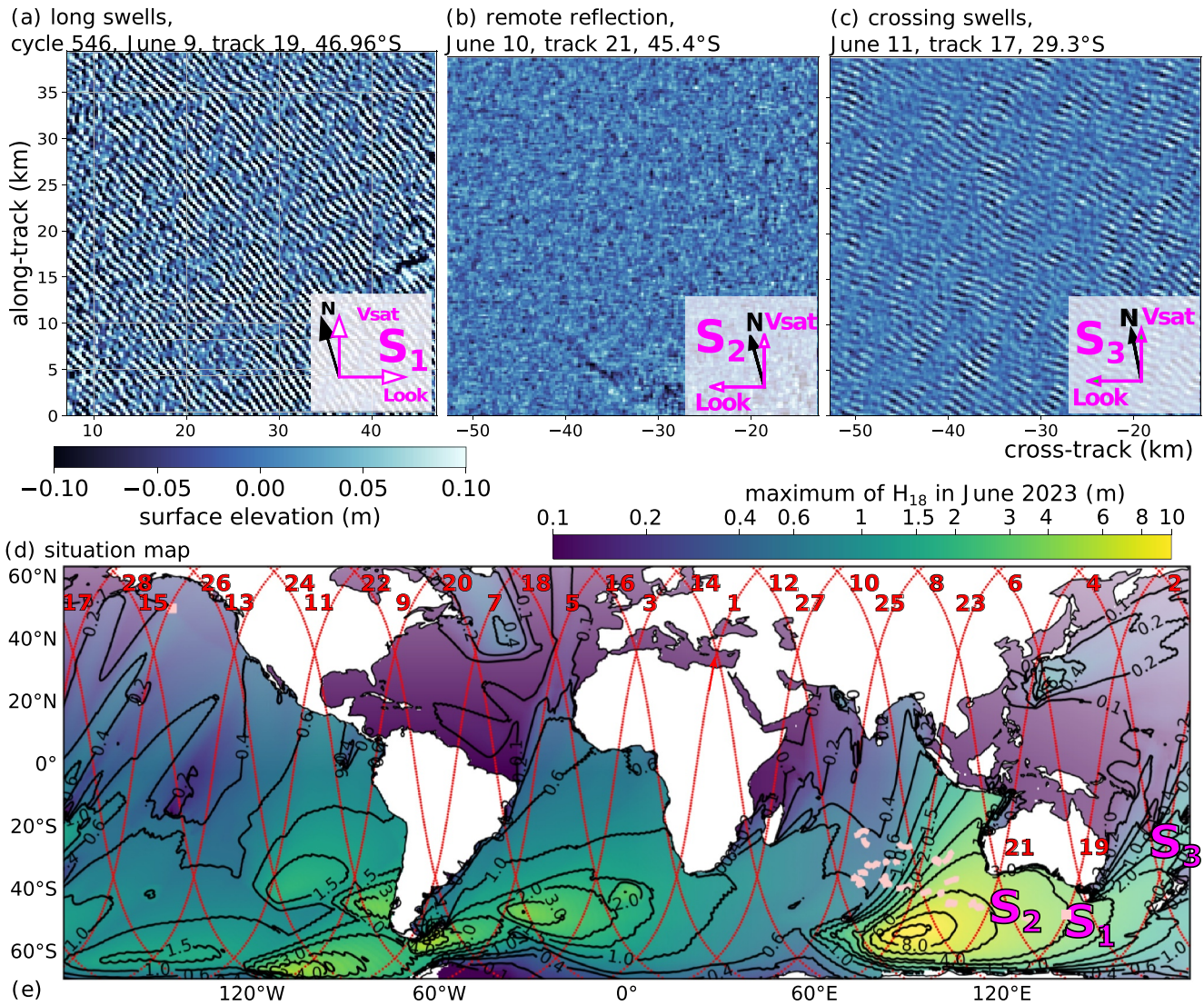


Figure 1. (a–c) Samples (40 km across) of the sea surface elevation (sea surface height) field relative to the reference geoid and detrended over 5 km tiles. Arrows indicate the direction of North (N), satellite flight (Vsat) and radar look direction (Look). The location of these samples, around Australia, are marked S_1 , S_2 , S_3 . Background colors in panel (d) show the maximum modeled value of H_{18} for the entire month of June 2023, overlaid with Surface Water Ocean Topography ground tracks (red lines, numbered from 1 to 27) and a selection of in situ buoys (pink lines in Indian Ocean and squares along tracks 15 and 19).

backscatter (σ_0) and SSH with a 250 m pixel size across a 120 km swath (with a center gap of 20 km). Figure 1 shows three samples of the ocean surface elevation, labeled S_1 – S_3 , each 40 km across.

These samples range from an apparently simple swell case in Figure 1a to barely visible features with a shorter wavelength in Figure 1b, and crossing swells in Figure 1c. We will quantify the magnitude of these waves with H_{18} , the wave height for waves longer than 18 s. Using buoy or model data this is defined as 4 times the square root of the integral of the wave frequency spectrum $E(f)$ from a frequency $f_{\min} = 1/30$ s to a frequency $f_{\max} = 1/18$ s. For SWOT data, this is taken as 4 times the square root of the integral—restricted to swell signals—of the wavenumber spectrum $E(k_x, k_y)$ for a spatial frequency $k = \sqrt{k_x^2 + k_y^2} < 2$ cycles per kilometer (cpk), that is, wavelengths larger than 500 m.

The long waves in Figures 1a–1c are all coming from the same storm. That storm was the most powerful on the globe for the months June–August 2023 as illustrated on Figure 1d. The maximum value of H_{18} exceeded 10 m, and the total significant wave height reached $H_s = 17.2$ m at 54°S, 86°E and 15:00 UTC on June 6, according to a wave model hindcast (Ardhuin & Accensi, 2024).

We expect that SWOT data will bring fresh insights on a wide range of physical processes from the generation of waves in storms to their propagation over currents and shallow topography. From March 2023 to July 2023, SWOT acquired data over the same orbit every 23.8 hr. We use that data to illustrate SWOT's wave-resolving capability, and provide the first validation of SWOT swell measurements (sample S_1), large scale evidence of coastal wave reflection (sample S_2) and island scattering (sample S_3). Reflection is locally relevant for nearshore morphodynamics, and probably dominant at global scales for the generation of microseisms with frequencies around 0.1 Hz (Ardhuin & Roland, 2012). Scattering by shallow water around small islands has not yet been explored scientifically, but traditional navigators from the Marshall Islands know this effect very well and use it for detecting islands beyond the horizon (Genz et al., 2009). Here we perform a similar detection using evidence of waves arriving from the 15 km wide Norfolk Island group located 300 km from a SWOT wave measurement. In Section 2 we detail an automatic method for retrieving swell parameters that works well for cases like sample S_1 . In Section 3 we discuss samples S_2 and S_3 that we interpret as evidence for coastal reflection and scattering. Conclusions and perspectives follow in Section 4.

2. Interpretation and Validation of SWOT Long Wave Signals

2.1. SWOT Processing and Analysis

We have used the Low Resolution (LR) “Unsmoothed” SWOT product (SWOT project, 2023), from the KaRIN interferometer, with pixels posted at approximately 250 m in each direction. In LR mode, the interferogram, whose phase is ultimately converted to surface elevation, is averaged on-board using a 500 m-wide filter. This filter combines with an effective point target response, so that the SWOT data is a convolution of the true SSH. The same convolution is performed on the single-channel powers to produce σ_0 on the same grid. To first order, components of the sea level power spectral density (PSD) at any spatial frequency (k_x, k_y) should be equal to the wave spectrum multiplied by a transfer function $G(k_x, k_y)$. We have chosen the x -axis oriented cross-track and the y -axis along-track. As we illustrate in this paper, the Unsmoothed KaRIn product resolves long swells, although with an amplitude heavily suppressed: as an example, G is typically 0.2 for cross-track propagating waves with $k_x = 1$ cpk and $k_y = 0$ meaning that for this wavelength of 1 km, the true amplitude of waves is larger than the amplitude of the SSH field by factor $1/\sqrt{0.2} = 2.2$.

Also, Doppler Beam formation in the presence of random velocities along the line of sight leads to a loss of resolution in the azimuth direction giving a multiplicative term $\exp(-k_y^2 \lambda_c^2)$ that is included in G , where λ_c is the same azimuthal cut-off wavelength as any other SAR imaging systems, and is a function of the mean wave period $T_{m0,2}$ and significant wave height H_s (Stopa et al., 2015). More details are given in the Supporting Information (see Figure S1 in Supporting Information S1 for G and its different components). Finally, because of the radar integration of echoes on iso-range surfaces, wave signals are generally distorted by the non-linear mapping from range to the cross-track dimension x . That “range bunching”, also called “surf board” effect (Peral et al., 2015), is strongest near storms.

For the cases shown in Figure 1, we expect that range bunching can be neglected and we estimate the wave spectrum E from the SWOT SSH PSD E_S as

$$E(k_x, k_y) = E_S(k_x, k_y)/G. \quad (1)$$

Our processing starts with computing the SSH PSD from the largest possible continuous square region in the SWOT swath, using 40 km by 40 km samples (as in Figure 1), in the middle of each left and right sub-swath, using a two-dimensional Welch (1967) method with tiles of 5 by 5 km and 50% overlap. This provides coarse spectra at low wavenumbers (as in Figure 2), but very accurate spectral densities and SSH- σ_0 cross spectra, with 128 degrees of freedom. The only delicate operation is to define a “swell mask” where Equation 1 is valid, avoiding parts of the spectrum with strong non-linear contributions around $k = 0$. For automatic processing, we rely on the expected coherence between the SSH and σ_0 , as shown in Figures 2g–2i.

We identify as well those components that have a σ_0 -SSH coherence higher than 0.05, and we dilate that region of the spectrum by one pixel to facilitate comparison with model output that may have slightly shifted peaks. This works well for the easy cases such as sample S_1 .

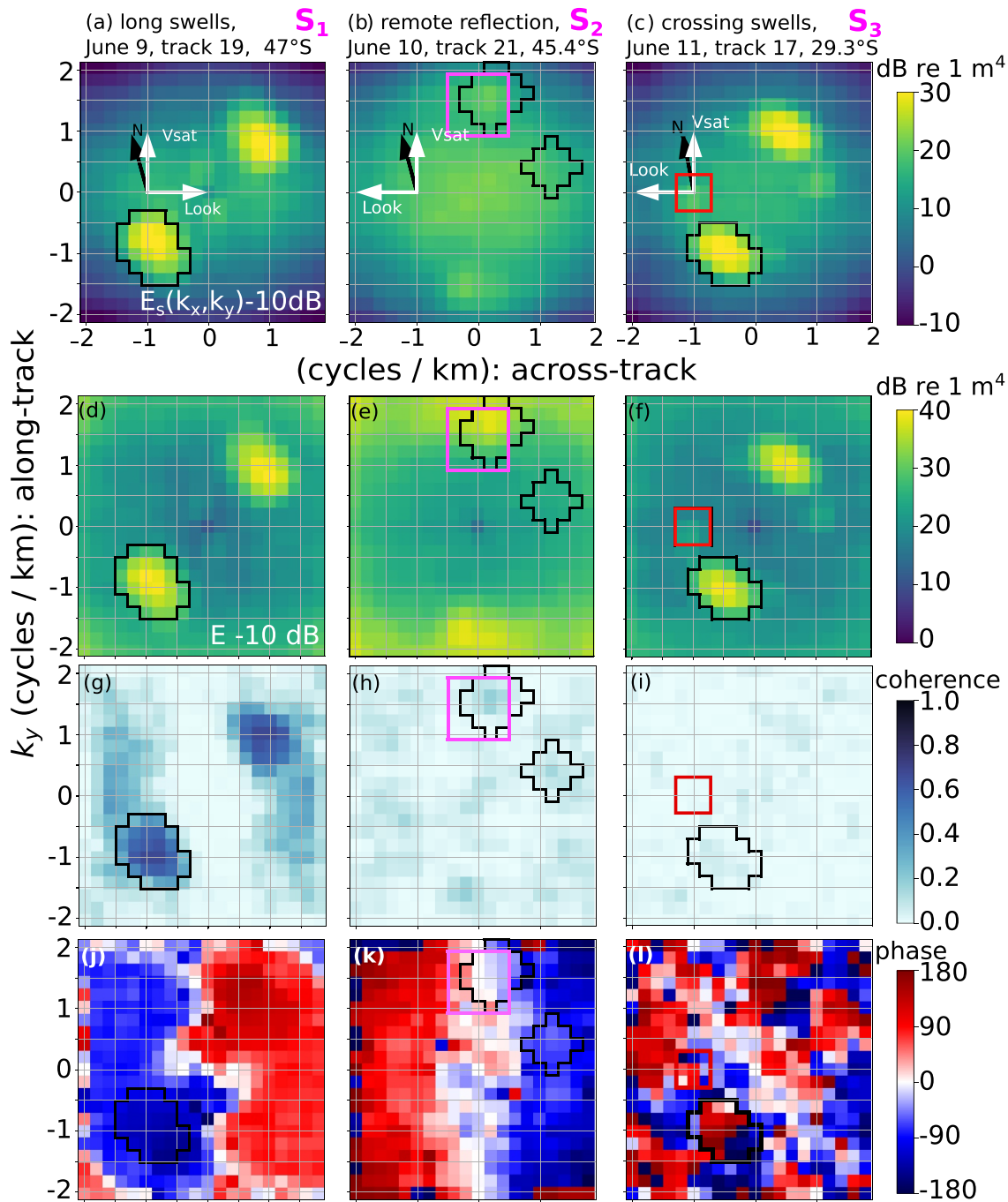


Figure 2. Top: power spectral density $E_S(k_x, k_y)$, second line: after filter correction $E(k_x, k_y) = E_S(k_x, k_y)/G$, third line: coherence from the σ_0 -SSH cross spectra, bottom line: associated phase. The black polygons show the edge of the “swell mask” using an automatic method: waves in the mask are in the direction from which they are propagating. Colored polygons in panels (b–d) are alternative swell masks defined a priori.

Finally, we restrict our swell mask to directions from which the waves arrive. For this we assume that for any wavelength and direction there are no waves in the opposite direction, and we use the phase of the SSH- σ_0 cross-spectrum to determine the direction. For waves propagating in the cross-track direction, σ_0 is maximum on the slope of the wave facing the radar, hence a cross-spectrum phase near 90° (red) for $k_x > 0$ and -90° (blue) for $k_x < 0$. Doppler processing on KaRIN modifies the maps of SSH and σ_0 : compared to a true geographical mapping, the velocity bunching effect displaces the ocean surface along the satellite track, which produces oscillations of σ_0 . These σ_0 oscillations are out of phase with the SSH for waves that propagate in the direction of the

satellite flight (Collard et al., 2022), hence a darker tone of red or blue in the cross-spectrum phase (Figures 2j and 2l). When waves propagate in the direction opposite to the satellite motion, SSH and σ_0 are in phase, giving a lighter tone of red or blue, as is the case in Figure 2k. This expected phase relationship indicates that the dominant swell direction was from the South in sample S_1 and S_3 (darker color, satellite flies to the North) and from the North for the magenta component in sample S_2 (lighter color). For waves propagating exactly in the cross-track direction, this method cannot separate between waves from the left or from the right (red box in Figure 2c).

2.2. Validating SWOT Resolved Wave Heights, Wavelengths and Directions

Because few buoys are within or near the SWOT swath, we use a two-step validation. To validate SWOT we use a numerical wave model simulation, that provides a complete spatial coverage (Ardhuin & Accensi, 2024). This model uses the configuration T707GQM described in Alday and Ardhuin (2023), and has been extensively validated with satellite altimeter and in situ buoy data. The spatial resolution is 0.5 by 0.5°, with a 15° angular resolution and exponentially spaced discrete frequencies, with a relative increment of 1.1 from one frequency to the next. Two features of this model make it unique: it includes coastal reflections even if very crudely, and it uses accurate nonlinear four-wave interactions (Gagnaire-Renou et al., 2010; Lavrenov, 2001).

As models can have large scale biases on swell parameters, first we use buoy data to validate this numerical wave model. Away from islands and major currents, swell fields are expected to vary smoothly over large scales (Delpy et al., 2010). A few buoys, even hundreds of kilometers from a SWOT swath, measure a model bias on H_{18} that is relevant to estimate the bias in that SWOT swath. The Southern Ocean Flux Station (SOFS) was positioned in the right swath of SWOT track 19, at 47.15°S 141.3°E. It is equipped with a dual-frequency geodetic quality Global Navigation Satellite System (GNSS) receiver, providing accurate wave measurements (Hay et al., 2023). The low frequencies of the heave spectrum have a white noise level around 0.01 m²/Hz, corresponding to a noise floor of 10 cm for low frequency swell heights. Spotter buoys (Raghukumar et al., 2019) from South-East Indian ocean provide a good sampling close to the storm (Houghton et al., 2024). These buoys use the less noisy GPS velocities instead of vertical positions, and thanks to their free drift and in spite of a lower quality GPS receiver compared to the SOFS mooring, they also achieve a noise floor of the order of 10 cm for H_{18} . Spotter buoys data are processed with a high pass 4th order Butterworth filter that removes spurious energy below the critical filter frequency of 0.033 Hz. This has a less than 0.1 dB impact for wavelengths shorter than 2 km and can thus be neglected. Additional data corresponding to sample S_4 (Figures S2–S3 in Supporting Information S1), were obtained from the moored Coastal Data Information Program station 166 located at 49.9 N 145.2 W (Thomson et al., 2013).

Data transmission constrains the spectral resolution of the Spotter buoys to 0.01 Hz. The model output was interpolated on the same Spotter frequency grid and H_{18} was estimated from the sum of the wave spectrum over the lowest 3 frequency bands, corresponding to a cut-off frequency of 0.0537 Hz (a period of 18.6 s). The peak of the swell event happens on June 6 for the region East of 90°E and South of 50°, and at later times, up to June 10 at the location of sample A, as the swell propagates to the East and North. Figure 4a shows that the model is generally consistent with buoy data when the local maximum value of H_{18} occurs. One exception is to the North-West of the model 1.0 m contour, where the model underestimates H_{18} by up to a factor 2. This result is specific to our use of accurate nonlinear wave parameterization (Lavrenov, 2001) and probably reveals deficiencies on the parameterization of other wave evolution processes in storms (Alday & Ardhuin, 2023). This topic is beyond the scope of the present paper. To the South of 40°S, the model slightly overestimates the maximum values of H_{18} .

Time series in Figures 3b–3c reveal more details. At buoy 010,379 (panel b), the agreement is generally good on June 8, followed by a model underestimation on June 9 and 10, except for the model with coastal reflection after 06:00 UTC on June 10, with model and buoy giving values around 20 cm. Without SWOT data, we would have discarded this as a coincidence. Directional buoy parameters are too noisy for such low wave heights and long period and do not provide a reliable estimate of the mean wave direction. A similar 20 cm reflected component is predicted by the model at the location of sample S_2 , consistent with buoy energy levels, and the model even predicts up to 40 cm along SWOT tracks 8 and 19 near sample S_1 .

We now compare SWOT data with buoy and model values. The modeled spectra are transformed to be comparable to the SWOT SSH spectra shown in Figure 2: Each spectrum is (a) regridded in wavenumber space to a resolution 3 times finer than in Figure 2 and for a larger domain from -4 to 4 cpk in both directions, (b) made centrally symmetric, (c) multiplied by G , (d) folded to the interval $[-2, 2]$ cpk to reproduce aliasing, (e) block-averaged to the same resolution as in Figure 2 (0.2 cpk along the x direction) to produce a filtered spectrum $E_s(k_x)$,

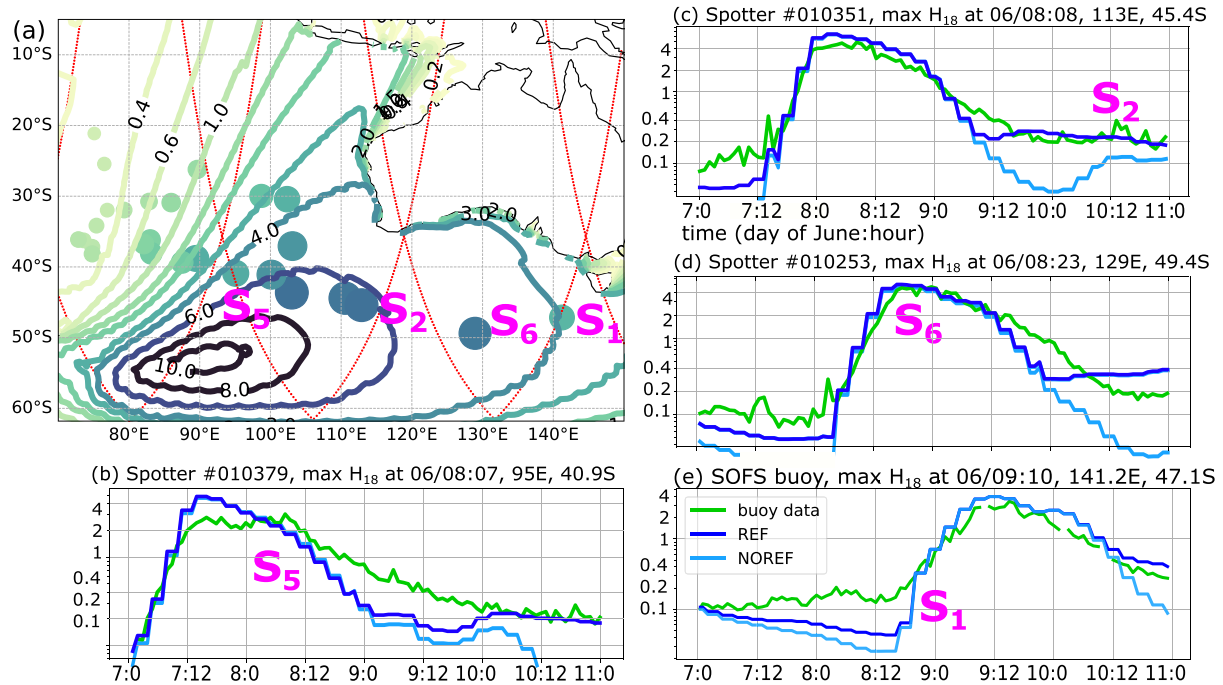


Figure 3. (a) Map showing the maximum value of H_{18} for June 6 to 12 June 2023 from the Spotter buoys (dots and written values from 0.7 to 4.9 m), and from the wave model (contours). Thick contours show the model maximum between June 1 and June 12. Locations of Surface Water Ocean Topography (SWOT) sample data are indicated by S_1 – S_6 (b–e) time series of H_{18} at Spotter buoys with identification number 010,379, 010,351 and 010,253, and Southern Ocean Flux Station buoy, and co-located model values, these buoys are closest to SWOT data samples, respectively. Light blue lines “NOREF” corresponds to the same model without coastal reflection.

k_y), and (f) divided by G to give an estimate of $E(k_x, k_y)$. From these SWOT and model spectra, H_{18} is computed from twice the spectrum in the swell mask, to account for double-sidedness. The swell direction θ_{18} is taken as the direction of the energy-weighted mean wavenumber vector, and the wavelength L_{18} as the ratio of zeroth and first moment of the two-dimensional masked wavenumber spectrum (Ardhuin, 2024). We note that the azimuth cut-off filter associated with velocity bunching, which is part of the transfer function G , requires some estimation of the root mean square orbital velocity w_{rms} , including waves not resolved by SWOT. We use the modeled w_{rms} , which was validated to be within 10% of buoy-derived values.

We start with a simple example: sample S_1 of the SWOT track number 19 around the SOFS mooring, for cycle 546 on June 9, 2 UTC, as shown in Figure 1a. The 1.1 m value for H_{18} is consistent with buoy and model data. Figure 4a gives a broader context (Movies S1 and S2 for more details). Sample S_1 has a mean wavelength of 760 m, and this value increases along the SWOT track toward the Australian coast, where it exceeds 1,000 m in deep water, corresponding to a wave period $T = 25.3$ s. As SWOT flies to the North, it catches up with the swell forerunners that have traveled faster and further. This is consistent with linear wave dispersion that gives a deep water group speed $C_g = gT/(4\pi)$ (Munk, 1947). Our SWOT-derived estimate of H_{18} closely follows the model value decreasing from 1.0 m to under 10 cm. To the South, we note that between latitudes 46 and 53°S, the mean direction θ_{18} veers by $\pm 6^\circ$. Since the left and right swath give two independent measurements at locations separated by 60 km, their correlation shows that these fluctuations in wave direction are not random but associated with features of the wave field. The local minimum of H_{18} from SWOT, at 48°S, is consistent with refraction over a current jet located upwave of the measurement location, similar to cases in Drake Passage discussed by Ardhuin et al. (2017). The maximum rotation of the wave direction occurs at locations consistent with that upwave current and the local current maximum (Villas Bôas & Young, 2020). Currents were not taken into account in our model simulation.

South of 50°S, the model overestimates the SWOT H_{18} values, which can be due (in part) to a model bias in that region, or a bias in our estimate of the G transfer function for wavelengths under 700 m and in the presence of a strong windsea. In sample S_1 this wind sea, unresolved in the LR SWOT data, gives a total wave height of 5.1 m as measured by the buoy.

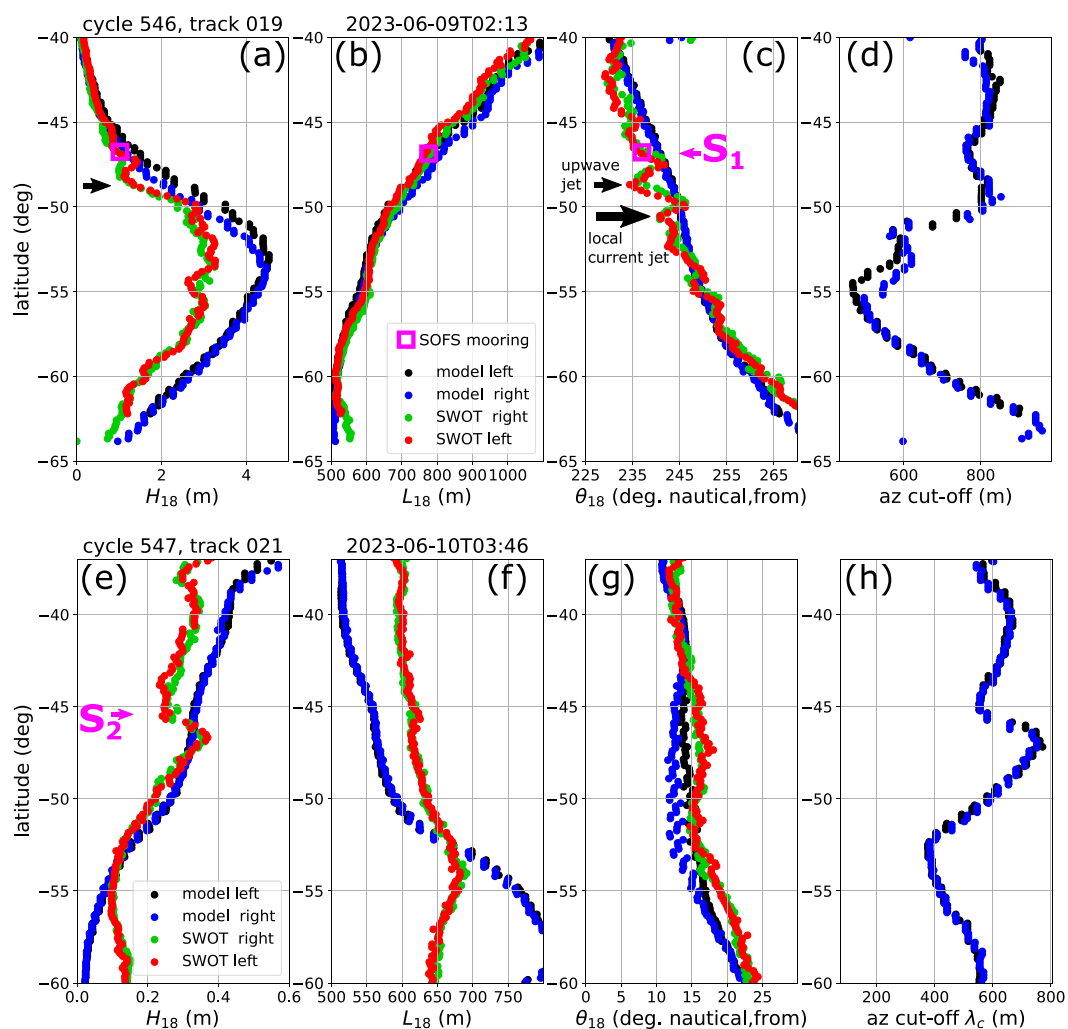


Figure 4. Examples of (a) swell height H_{18} , (b) swell wavelength L_{18} , (c) swell direction θ_{18} and (d) azimuthal cut-off λ_c along Surface Water Ocean Topography track 19, South of Australia on June 9th, around 2:10 UTC. Same quantities in panels (e–h) for track 21, South of Australia on June 11th.

3. Coastal Reflection and Scattering: From Big to Small Islands

Guza and O’Reilly (2001) performed the only study that found evidence of coastal reflection in wave heights measured in deep water at a location sheltered from the offshore direct wave propagation. Otherwise reflected waves have been incredibly challenging to observe. In general, large scale shoreline reflection coefficients for the wave energy are very poorly known and poorly constrained by microseism measurements, giving energy reflection coefficients values $0.02 < R^2 < 0.1$ (Stutzmann et al., 2012). Our numerical simulation with a constant $R^2 = 0.1$ was thus expected to overestimate reflection.

Sample S_2 is not the most obvious case of reflected waves in SWOT data, but it is easy to analyze quantitatively due to the absence of incident waves at the same time (they can be seen on the previous day). Unfortunately the directional parameters from the buoy are noisy and the directional spread, around 60° (Figure S6 in Supporting Information S1), could be interpreted as a nearly isotropic directional spectrum or can be biased high due to noise (O’Reilly et al., 1996). In contrast, the SWOT cross-spectrum phase with values under 45° in Figure 2k for the swell peak, clearly indicates a dominant wave direction from the North.

For sample S_2 , our automatic processing gives SWOT wave heights that are biased high because, once corrected for the transfer function G , the swell peak blends with the noise on the edge of the spectral domain at $(k_x = 0, k_y = 2)$ (Figure 2e). As a result we have used a fixed “alternative mask”, the magenta box in Figure 2b.

It is noteworthy that L_{18} clearly increases from 570 m at 41°S to 670 m at 52°S, consistent with a dispersive propagation of waves from North to South. Overall, the buoy and SWOT data are consistent with the model reflected components coming from the region around Cape Leeuwin. Our model parameter choice $R^2 = 0.1$ is surprisingly accurate for this region and those waves.

It is possible that the opposite trend of L_{18} at latitudes 57–54°S, increasing from South to North, is actually due to reflections off small icebergs that are very numerous around 62°, and appear as strong bright/dark dipoles in maps of σ_0 (Movie S2). For other regions, such as the Great Australian Bight, the model overestimation of H_{18} at buoy 010,253 on June 10 (Figure 3d), and the lower SWOT values on track 19 (not shown) suggest that the reflection coefficient should be smaller, probably associated to fewer cliffs and less steep beaches along the shoreline encountered by these reflected waves (Ardhuin & Roland, 2012).

The presence of waves is much easier to detect for the longest swell components and when the noise level is lower, such as in sample S_3 , acquired North of New Zealand on track 17. In that case, the main peak (within the black polygon on Figure 2c) is associated with a height $H_{18} = 0.30$ m for both model and SWOT. A weaker component coming from East or West is barely visible, and is highlighted by the red square in Figure 2f. That cross-track component is found consistently along the SWOT track from 30.7 to 28.7°S. Outside of that area, the SSH spectral density in the red square in Figure 2c is 18–20 dB (60–100 m^4), giving a background noise wave height of 2 cm. This value rises to only 4 cm in sample S_3 : subtracting the background noise gives a wave height corrected to $\sqrt{(4^2 - 2^2)} \approx 3$ cm.

Where are these 3 cm waves coming from? Although we cannot lift the 180° direction ambiguity from sample S_3 alone, the rotation of the mean direction between neighboring samples is consistent with a localized source to the West of the SWOT track, with waves veering from an azimuth of 280° to 260° over a distance of 100 km along the track (Movie S4). Assuming a circular wave front, this rotation would correspond to a radius of 270 km. At this latitude, the SWOT track number 4 lies 300 km to the West of track 17, providing data 13 hr after sample S_3 . Indeed, along track 4, from 29.4 to 28.4°S, SWOT covers part of the shelf of Norfolk Island, which is much wider (100 km) than the island itself (15 km). SWOT swells have a much broader directional spectrum at the edge of the shelf (see sample S_7 , Figures S2–S3 in Supporting Information S1 and Movie S4). Therefore the crossing sea pattern in S_3 can only be reasonably explained by refraction over the shelf surrounding Norfolk island, an effect not yet considered in global ocean wave models.

The wider variety of wave patterns in both SSH and σ_0 fields, and amazing uninterrupted coverage provided by SWOT is more fully visualized in Movies S1–S4, and Figure S2 in Supporting Information S1. Sample S_4 taken on June 17 near station PAPA, 17,000 km away from the storm, is shown in Supporting Figure S2 in Supporting Information S1.

4. Conclusions and Perspectives

As demonstrated by Fu et al. (2024), SWOT resolution and accuracy is providing an order of magnitude improvement on the measurement of “ocean topography”, compared to nadir satellite altimeters. That ocean topography contains the large scale component of the surface elevation that is related to currents by the geostrophic balance. However, SWOT data actually contains many other components of ocean dynamics, in both maps of surface elevation and radar backscatter. We have shown that SWOT data contains useful and accurate information on swell height, wavelength and direction, for the infrequent but important cases with wavelengths in the range 500–1,050 m. The swell detection level varies with wavelength and other factors: in calm areas a swell height of 3 cm and 1 km wavelength was detected, far beyond the reach of existing remote sensing techniques using radar or optical imagery, and even beyond the reach of standard surface oceanographic buoys. A detailed validation will require instruments and processing more precise than standard wave buoys. Other instruments such as underwater pressure recorders are sensitive enough but usually mounted on the bottom and can only measure swells in shallow enough areas that are not necessarily representative of open ocean conditions (Snodgrass et al., 1966).

The main limitation of the global SWOT data is the 250 m pixel size. Computing a surface elevation spectrum on board, which could have given access to shorter waves before data is averaged, is not feasible on SWOT but may be possible on future similar satellites. This additional information would be most useful for mapping shorter

swells and refining the surface height error model. That possibility will be investigated using SWOT High Resolution data, available in many coastal regions and few offshore locations. Besides, a further analysis of the performance of SWOT for swell mapping will benefit from ongoing work to define a model for the SWOT “background noise”. This noise contains many effects including a nonlinear transformation of the wave spectrum (Peral et al., 2015), and it may have a level comparable to the swell signal studied here, as shown in Figures S2 and S3 in Supporting Information S1 with samples S_5 and S_6 .

SWOT data is opening a new era of measurements for kilometer-long waves allowing many new applications. For example, SWOT is uniquely capable of mapping swell fields reflected or scattered from islands of all sizes, a phenomenon that is still poorly quantified and modeled. That capability will lead to a clear improvement of models for microseism sources, which are limited by our knowledge of ocean wave reflection at coasts or icebergs. These microseism models are now used to map the Earth's mantle (Kato & Nishida, 2023; Nishida & Takagi, 2016; Tomasetto et al., 2024), and may also be used to probe stratospheric winds (De Carlo et al., 2021; Vorobeva et al., 2024). Conversely, by providing a calibration point for recent swell events, SWOT data can now be used to further constrain historical records of ocean storms based on microseism records (Aster et al., 2023).

Data Availability Statement

The SWOT data used in the study are version 2.0 of Level-2 KaRIn Low Rate SSH Unsmoothed (SWOT project, 2023). The SWOT L2_LR_SSH data product is produced and made freely available by the joint SWOT (NASA/JPL and CNES) project. L2_LR_SSH product quality is not final and will be affected by some evolutions as the SWOT project team makes progress on science data processing algorithms and instrument calibrations. SWOT project (2023). The buoy data used for model validation (Houghton et al., 2024), and the model output (Ardhuin & Accensi, 2024) are available from SEANOE under CC-BY v4 licence. The swellSWOT tool box used for present analyses is also available via SEANOE under CC-BY v4 licence (Ardhuin, 2024).

Acknowledgments

We are very grateful for suggestions by T. Farrar, B. Chapron, T. Postec, and two anonymous reviewers, and technical support from M. Accensi. This research was made possible by the dedication of the entire SWOT mission crew and the support of U.S. and French taxpayers. SOFS data were sourced from Australia's Integrated Marine Observing System (IMOS)—IMOS is enabled by the National Collaborative Research Infrastructure Strategy (NCRIS).

References

- Alday, M., & Ardhuin, F. (2023). On consistent parameterizations for both dominant wind-waves and spectral tail directionality. *Journal of Geophysical Research*, 128(4), e2022JC019581. <https://doi.org/10.1029/2022JC019581>
- Ardhuin, F. (2024). Tools for the analysis of swells in swot satellite data - Version 1 [Dataset]. SEANOE. <https://doi.org/10.17882/99836>
- Ardhuin, F., & Accensi, M. (2024). Numerical wave model output for June 2023, co-located with swot and buoy data for the analysis of swells from storm Rosemary [Dataset]. SEANOE. <https://doi.org/10.17882/99783>
- Ardhuin, F., Chapron, B., Collard, F., Smith, M., Stopa, J., Thomson, J., et al. (2017). Measuring ocean waves in sea ice using SAR imagery: A quasi-deterministic approach evaluated with sentinel-1 and in situ data. *Remote Sensing of Environment*, 189, 211–222. <https://doi.org/10.1016/j.rse.2016.11.024>
- Ardhuin, F., Collard, F., Chapron, B., Girard-Ardhuin, F., Guitton, G., Mouche, A., & Stopa, J. (2015). Estimates of ocean wave heights and attenuation in sea ice using the SAR wave mode on Sentinel-1A. *Geophysical Research Letters*, 42(7), 2317–2325. <https://doi.org/10.1002/2014GL062940>
- Ardhuin, F., & Roland, A. (2012). Coastal wave reflection, directional spreading, and seismo-acoustic noise sources. *Journal of Geophysical Research*, 117(C11), C00J20. <https://doi.org/10.1029/2011JC007832>
- Aster, R. C., Ringler, A. T., Anthony, R. E., & Lee, T. A. (2023). Increasing ocean wave energy observed earth's seismic wavefield since the late 20th century. *Nature Communications*, 14(1), 6984. <https://doi.org/10.1038/s41467-023-42673-w>
- Collard, F., Marié, L., Nougier, F., Kleinherenbrink, M., Ehlers, F., & Ardhuin, F. (2022). Wind-wave attenuation in arctic sea ice: A discussion of remote sensing capabilities. *Journal of Geophysical Research*, 127(7), e2022JC018654. <https://doi.org/10.1029/2022JC018654>
- Darbyshire, J. (1950). Identification of microseismic activity with sea waves. *Proceedings of the Royal Society of London*, (Vol. 202, 439–448).
- De Carlo, M., Hupe, P., Le Pichon, A., & Ardhuin, F. (2021). Global microbarom patterns: A first confirmation of the theory for source and propagation. *Geophysical Research Letters*, 48(3), e2020GL090163. <https://doi.org/10.1029/2020GL090163>
- Delpy, M., Ardhuin, F., Collard, F., & Chapron, B. (2010). Space-time structure of long swell systems. *Journal of Geophysical Research*, 115(C12), C12037. <https://doi.org/10.1029/2009JC005885>
- Fu, L., Pavelsky, T., Cretaux, J., Morrow, R., Farrar, J. T., Vaze, P., et al. (2024). The surface water and ocean topography mission: A breakthrough in radar remote sensing of the ocean and land surface water. *Geophysical Research Letters*, 51(4), e2023GL107652. <https://doi.org/10.1029/2023GL107652>
- Gagnaire-Renou, E., Benoit, M., & Forget, P. (2010). Ocean wave spectrum properties as derived from quasi-exact computations of nonlinear wave-wave interactions. *Journal of Geophysical Research*, 115(C12), C12058. <https://doi.org/10.1029/2009JC005665>
- Gallet, B., & Young, W. R. (2014). Refraction of swell by surface currents. *Journal of Marine Research*, 72(2), 105–126. <https://doi.org/10.1357/002224014813758959>
- Genz, J., Aucan, J., Merrifield, M., Finney, B., Joel, K., & Kelen, A. (2009). Wave navigation in the Marshall Islands. *Oceanography*, 22(2), 234–245. <https://doi.org/10.5670/oceanog.2009.52>
- Guza, R. T., & O'Reilly, W. C. (2001). *Wave prediction in the Santa Barbara channel (Tech. Rep.)*. U. S. Department of the Interior, Mineral Management Service, Pacific OCS Region. Retrieved from <http://www.coastalresearchcenter.ucsb.edu/cmi/files/2001-055.pdf>
- Hanafin, J., Quilfen, Y., Ardhuin, F., Sienkiewicz, J., Queffelec, P., Obrebski, M., et al. (2012). Phenomenal sea states and swell radiation: A comprehensive analysis of the 12–16 February 2011 North Atlantic storms. *Bulletin of the American Meteorological Society*, 93(12), 1825–1832. <https://doi.org/10.1175/BAMS-D-11-00128.1>

- Hasselmann, K., Raney, R. K., Plant, W. J., Alpers, W., Shuchman, R. A., Lyzenga, D. R., et al. (1985). Theory of synthetic aperture radar ocean imaging: A MARSEN view. *Journal of Geophysical Research*, *90*(C3), 4659–4686. <https://doi.org/10.1029/jc090ic03p04659>
- Hauser, D., Tourain, C., Hermozo, L., Alraddawi, D., Aouf, L., Chapron, B., et al. (2021). New observations from the SWIM radar on-board CFOSAT: Instrument validation and ocean wave measurement assessment. *IEEE Transactions on Geoscience and Remote Sensing*, *59*(1), 5–26. <https://doi.org/10.1109/tgrs.2020.2994372>
- Hay, A., Watson, C., Legresy, B., King, M., & Beardsley, J. (2023). In situ validation of altimetry and CFOSAT SWIM measurements in a high wave environment. *Journal of Atmospheric and Oceanic Technology*, *40*(10), 1137–1152. <https://doi.org/10.1175/JTECH-D-23-0031.1>
- Houghton, I., Arduin, F., & Hay, A. (2024). Spotter buoy data for June 6 2023 storm Rosemary [Dataset]. *SEANOE*. <https://doi.org/10.17882/99739>
- Husson, R., Arduin, F., Chapron, B., Collard, F., & Balanche, A. (2012). Swells throughout the Pacific: A combined view using the global seismic network and Envisat's wave mode ASAR data. *Geophysical Research Letters*, *39*(15), L15609. <https://doi.org/10.1029/2012GL052334>
- Jackson, F. C., Walton, W. T., & Peng, C. Y. (1985). A comparison of in situ and airborne radar observations of ocean wave directionality. *Journal of Geophysical Research*, *90*(C1), 1005–1018. <https://doi.org/10.1029/jc090ic01p01005>
- Kato, S., & Nishida, K. (2023). Extraction of mantle discontinuities from teleseismic body-wave microseisms. *Geophysical Research Letters*, *50*(18), e2023GL105017. <https://doi.org/10.1029/2023GL105017>
- Lavrenov, I. V. (2001). Effect of wind wave parameter fluctuation on the nonlinear spectrum evolution. *Journal of Physical Oceanography*, *31*(4), 861–873. [https://doi.org/10.1175/1520-0485\(2001\)031<0861:EOWWPF>2.0.CO;2](https://doi.org/10.1175/1520-0485(2001)031<0861:EOWWPF>2.0.CO;2)
- Munk, W. H. (1947). Tracking storms by forerunners of swell. *Journal of Meteorology*, *4*(2), 45–57. [https://doi.org/10.1175/1520-0469\(1947\)004<0045:tsfos>2.0.co;2](https://doi.org/10.1175/1520-0469(1947)004<0045:tsfos>2.0.co;2)
- Munk, W. H., Miller, G. R., Snodgrass, F. E., & Barber, N. F. (1963). Directional recording of swell from distant storms. *Philosophical Transactions of the Royal Society of London - A*, *255*, 505–584.
- Nishida, K., & Takagi, R. (2016). Teleseismic S wave microseisms. *Science*, *353*(6302), 919–921. <https://doi.org/10.1126/science.aaf7573>
- O'Reilly, W. C., Herbers, T. H. C., Seymour, R. J., & Guza, R. T. (1996). A comparison of directional buoy and fixed platform measurements of Pacific swell. *Journal of Atmospheric and Oceanic Technology*, *13*(1), 231–238. [https://doi.org/10.1175/1520-0426\(1996\)013<0231:acodba>2.0.co;2](https://doi.org/10.1175/1520-0426(1996)013<0231:acodba>2.0.co;2)
- Peral, E., Rodriguez, E., & Esteban-Fernandez, D. (2015). Impact of surface waves on SWOT's projected ocean accuracy. *Remote Sensing*, *7*(11), 14509–14529. <https://doi.org/10.3390/rs71114509>
- Raghukumar, K., Chang, G., Spada, F., Jones, C., Janssen, T., & Gans, A. (2019). Performance characteristics of “Spotter,” a newly developed real-time wave measurement buoy. *Journal of Atmospheric and Oceanic Technology*, *36*(6), 1127–1141. <https://doi.org/10.1175/JTECH-D-18-0151.1>
- Snodgrass, F. E., Groves, G. W., Hasselmann, K., Miller, G. R., Munk, W. H., & Powers, W. H. (1966). Propagation of ocean swell across the Pacific. *Philosophical Transactions of the Royal Society of London*, *A249*, 431–497.
- Stopa, J. E., Arduin, F., Chapron, B., & Collard, F. (2015). Estimating wave orbital velocity through the azimuth cutoff from space-borne satellite. *Journal of Geophysical Research*, *130*, 7616–7634. <https://doi.org/10.1002/2015JC011275>
- Stutzmann, E., Schimmel, M., Arduin, F., Mangeney, A., & Patau, G. (2012). Modeling long-term seismic noise in various environments. *Geophysical Journal International*, *191*(2), 707–722. <https://doi.org/10.1111/j.1365-246X.2012.05638.x>
- SWOT project. (2023). Swot level-2 Karin low rate SSH unsmoothed, reprocessed version c products (v2.0) [Dataset]. *CNES*. <https://doi.org/10.24400/527896/A01-2023.016>
- Thomson, J., D'Asaro, E. A., Cronin, M. F., Rogers, W. E., Harcourt, R. R., & Shcherbina, A. (2013). Waves and the equilibrium range at ocean weather station P. *Journal of Geophysical Research*, *118*(11), 595–5962. <https://doi.org/10.1002/2013JC008837>
- Tomasetto, L., Boué, P., Stehly, L., Arduin, F., & Nataf, H.-C. (2024). On the stability of mantle-sensitive p-wave interference during a secondary microseismic event. *Geophysical Research Letters*, *51*(8). <https://doi.org/10.1029/2023GL108018>
- Villas Bôas, A. B., & Young, W. R. (2020). Integrated observations and modeling of winds, currents, and waves: Requirements and challenges for the next decade. *Journal of Fluid Mechanics*, *890*, R3. <https://doi.org/10.1017/jfm.2020.116>
- Vorobeva, E., Eggen, M. D., Midtjord, A. D., Benth, F. E., Hupe, P., Brissaud, Q., et al. (2024). Estimating stratospheric polar vortex strength using ambient ocean noise and stochastic-based machine learning. *Quarterly Journal of the Royal Meteorological Society*, *150*(762), 2712–2726. <https://doi.org/10.1002/qj.4731>
- Welch, P. D. (1967). The use of fast Fourier transform for the estimation of power spectra: A method based on time averaging over short, modified periodograms. *IEEE Transactions on Audio and Electroacoustics*, *15*(2), 70–73. <https://doi.org/10.1109/tau.1967.1161901>

References From the Supporting Information

- Almar, R., Bergsma, E. W. J., Thoumyre, G., Baba, M. W., Cesbron, G., Daly, C., et al. (2021). Global satellite-based coastal bathymetry from waves. *Remote Sensing*, *13*(22), 4628. <https://doi.org/10.3390/rs13224628>
- Hasselmann, K., & Hasselmann, S. (1991). On the nonlinear mapping of an ocean wave spectrum into a synthetic aperture radar image spectrum and its inversion. *Journal of Geophysical Research*, *96*(C6), 10713–10729. <https://doi.org/10.1029/91jc00302>
- Styles, B., & Dubois, P. (2023). *Surface water and ocean topography project algorithm theoretical basis document, long name: Level 1b Karin low rate interferogram science algorithm software*. Short name: LIB_LR_INTF (Tech. Rep. No. JPL D-105501). Retrieved from <https://podaac.jpl.nasa.gov/swot?tab=datasets-information§ions=about>